Electronic Supplementary Material (ESI) for ChemComm.
This journal is © The Royal Society of Chemistry 2021

Reversible Polymorphic Structural Transition of Crown-like Nickel Nanoclusters and Its Effect on Conductivity

Manju P. Maman,[a] Akashdeep Nath,[a] Anjusree S,[b] Bikas C. Das,[b] Sukhendu Mandal*[a]

[a]School of Chemistry, Indian Institute of Science Education and Research Thiruvananthapuram, Thiruvananthapuram, Kerala, India-695551; Email: sukhendu@iisertvm.ac.in

[b]School of Physics, Indian Institute of Science Education and Research Thiruvananthapuram, Thiruvananthapuram, Kerala, India-695551

Supporting Information Placeholder

1. Materials

Nickel (II) nitrate hexahydrate ($Ni(NO_3)_2 \cdot 6H_2O$, > 99.99 % metals basis), 2-Phenylethanethiol (PET, 98%), sodium borohydride ($NaBH_4$, 99.99 %, trace metal basis), tetraoctylammonium bromide (TOAB, 98%), *trans*-2-[3-(4-tert-butylphenyl)-2-methyl-2 propenylidene] malononitrile (DCTB, > 99.0 %) were purchased from Sigma Aldrich. Solvents used were MeOH (HPLC grade, 99.9 %, Spectrochem), ethanol (absolute, Emsure), Tetrahydrofuran (THF, HPLC grade, 99.9 %, Spectrochem), toluene (Tol, HPLC grade, 99.9 %, Spectrochem), Dimethylene chloride (DCM, HPLC grade, 99.9 %, Spectrochem), Milli-Q water.

2. Synthesis of Compound 1:

Nickel (II) nitrate hexahydrate ($Ni(NO_3)_2.6H_2O$, 0.1 mmol, 29 mg) and tetraoctylammonium bromide (TOAB, 0.3 mmol, 164 mg) was taken in the 100 mL round bottom (R.B) flask containing 20 mL THF (HPLC grade). The reaction mixture was allowed for 30 min stirring (for solubility). Followed by addition of 2-Phenylethanethiol (PET, 0.57 mmol, 76.34 μL). After one-hour sodium borohydride ($NaBH_4$, 1.23 mmol, 46.5 mg) dissolved in 5 mL of ice cold Milli-Q water was added quickly. The reaction mixture was allowed for 7 h stirring at ambient condition. Solvent was evaporated at room temperature, remaining residue was washed with ethanol thrice and extracted with 3 mL of Dimethylene chloride (DCM) solvent. The DCM solution of compound 1 was then centrifuged to remove unwanted residue.

Crystallization of compound 1:

DCM solution of compound **1** (3 mL) was layered with equal volume of absolute ethanol. After one small block like crystal was observed in side of the vial. The crystals were wash several times with ethanol for more purity.

Compound 2: The heating of compound **1** at 130 °C lead to the formation of compound **2**.

3. **Reversibility of the compound 2 to compound 1**

Compound **1** was obtained by dissolving compound **2** in 5 mL DCM solution, and then evaporated at 40 °C.

4. **X-ray Crystallography.** The single crystal X-ray diffraction data for both the clusters were collected on the Bruker Smart APEX II diffractometer equipped with CCD detector using monochromatic MoKα radiation (λ = 0.71073 Å) at room temperature. Unit cell parameters collection, data collection, integration, and scaling for the data were carried out by Bruker Apex II software.[1] SADABS was used for the numerical absorption correction.[2] Data reduction was conducted using Bruker SAINT suite.[3] SHELXT 2014[4] was used for the crystal structure solution and refined by the full matrix least squares method using SHELXL 2018[5] available in the WinGX program suite (version 2014.1).[6] Anisotropic refinement was used for all non-hydrogen atoms and hydrogen atoms were (positioned geometrically) refined isotropically using a riding model.

5. **Table S1** (a). Crystallographic parameters of the **1**

Parameters	**Compound 1**
CCDC	2053606
Empirical formula	$C_{48}H_{54}Ni_3S_6$
Formula weight	999.40
Crystal System	Monoclinic
Space Group	$P2_1/n$ (No. 14)

a (Å)	11.329 (5)
b (Å)	12.521 (6)
c (Å)	32.774 (15)
α (^{0})	90
β (^{0})	91.641(5)
γ (^{0})	90
Volume (Å^3)	4647 (4)
Z	4
Calculated density (mg/m^3)	1.428
θ range (^{0})	1.243 to 26.372
Absorption coefficient (mm^{-1})	1.505
Reflections collected	45697
Unique reflections	9509
Goodness of fit on F^2	1.167
Number of parameters	515
Final R indices [I > 2sigma(I)]	R_1 = 0.1093, wR_2 = 0.2651
R indices (all data)	R_1 = 0.1924, wR_2 = 0.3115

Table S1 (b). Selected Bond Lengths (Å) and Angles (deg) of the **1**

Ni(1)-S(1)	2.188(3)	Ni(1)-S(4)	2.191(3)
Ni(1)-S(5)	2.196(3)	Ni(1)-S(6)	2.207(3)
Ni(1)-Ni(3)#1	2.930(2)	Ni(2)-S(4)	2.188(3)
Ni(2)-S(3)	2.192(3)	Ni(2)-S(1)	2.195(3)

Ni(2)-S(2)	2.202(3)	Ni(2)-Ni(3)	2.830(2)
Ni(3)-S(5)#1	2.173(3)	Ni(3)-S(3)	2.192(3)
Ni(3)-S(2)	2.197(3)	Ni(3)-S(6)#1	2.227(3)
S(1)-Ni(1)-S(4)	82.44(12)	S(1)-Ni(1)-S(5)	97.46(13)
S(4)-Ni(1)-S(5)	171.70(13)	S(4)-Ni(1)-S(6)	98.61(13)
S(5)-Ni(1)-S(6)	82.72(12)	S(1)-Ni(1)-Ni(3)#1	125.78(11)
S(4)-Ni(1)-Ni(3)#1	138.38(10)	S(5)-Ni(1)-Ni(3)#1	47.55(8)
S(5)-Ni(1)-Ni(3)#1	47.55(8)	S(6)-Ni(1)-Ni(3)#1	48.93(9)
S(4)-Ni(2)-S(3)	176.67(13)	S(4)-Ni(2)-S(1)	82.36(13)
S(3)-Ni(2)-S(1)	98.48(13)	S(4)-Ni(2)-S(2)	98.51(13)
S(3)-Ni(2)-S(2)	81.54(13)	S(1)-Ni(2)-S(2)	164.73(13)
S(4)-Ni(2)-Ni(3)	132.49(11)	S(3)-Ni(2)-Ni(3)	49.80(9)
S(1)-Ni(2)-Ni(3)	119.15(11)	S(2)-Ni(2)-Ni(3)	49.86(9)
S(5)#1-Ni(3)-S(3)	176.76(14)	S(5)#1-Ni(3)-S(2)	96.61(13)
S(3)-Ni(3)-S(2)	81.65(12)	S(5)#1-Ni(3)-S(6)#1	82.75(12)
S(3)-Ni(3)-S(6)#1	99.52(13)	S(2)-Ni(3)-S(6)#1	168.18(14)
S(5)#1-Ni(3)-Ni(2)	130.77(10)	S(3)-Ni(3)-Ni(2)	49.79(9)
S(2)-Ni(3)-Ni(2)	50.03(9)	S(6)#1-Ni(3)-Ni(2)	122.34(10)
S(5)#1-Ni(3)-Ni(1)#1	48.20(9)	S(3)-Ni(3)-Ni(1)#1	135.02(11)
S(2)-Ni(3)-Ni(1)#1	123.45(10)	S(6)#1-Ni(3)-Ni(1)#1	48.33(9)

Table S2 (a). Crystallographic parameters of the **2**

Parameters	**Compound 2**
CCDC	2053607
Empirical formula	$C_{48}H_{54}Ni_3S_6$
Formula weight	999.40
Crystal System	Monoclinic
Space Group	$P2_1/n$ (No. 14)
a (Å)	17.295(16)
b (Å)	10.630(10)
c (Å)	25.80(2)
α (^{0})	90
β (^{0})	99.43(3)
γ (^{0})	90
Volume (Å^3)	4679(8)
Z	4
Calculated density (mg/m^3)	1.419
θ range (^{0})	1.323 to 28.523
Absorption coefficient (mm^{-1})	1.495
Reflections collected	66991
Unique reflections	11675
Goodness of fit on F^2	0.948
Number of parameters	515
Final R indices [I>2sigma(I)]	R_1 = 0.0691, wR_2 = 0.1483

R indices (all data)	$R_1 = 0.1683$, $wR_2 = 0.2055$

Table S2 (b). Selected Bond Lengths (Å) and Angles (deg) of the **2**

Ni(1)-S(2)	2.206(3)	Ni(1)-S(1)	2.213(2)
Ni(1)-S(5)#1	2.222(2)	Ni(1)-S(6)#1	2.225(2)
Ni(1)-Ni(3)#1	2.869(2)	Ni(2)-S(1)	2.196(2)
Ni(2)-S(4)	2.198(2)	Ni(2)-S(3)	2.217(2)
Ni(2)-S(2)	2.220(2)	Ni(2)-Ni(3)	2.919(3)
Ni(3)-S(4)	2.205(2)	Ni(3)-S(5)	2.207(2)
Ni(3)-S(6)	2.213(3)	Ni(3)-S(3)	2.216(3)
S(2)-Ni(1)-S(1)	81.74(8)	S(2)-Ni(1)-S(5)#1	97.52(8)
S(1)-Ni(1)-S(5)#1	174.06(7)	S(2)-Ni(1)-S(6)#1	172.94(7)
S(1)-Ni(1)-S(6)#1	98.86(8)	S(5)#1-Ni(1)-S(6)#1	82.61(8)
S(2)-Ni(1)-Ni(3)#1	125.72(7)	S(1)-Ni(1)-Ni(3)#1	135.43(7)
S(1)-Ni(1)-Ni(3)#1	135.43(7)	S(5)#1-Ni(1)-Ni(3)#1	49.41(6)
S(6)#1-Ni(1)-Ni(3)#1	49.56(7)	S(1)-Ni(2)-S(4)	177.58(7)
S(1)-Ni(2)-S(3)	98.57(8)	S(4)-Ni(2)-S(3)	81.44(8)
S(1)-Ni(2)-S(2)	81.80(8)	S(4)-Ni(2)-S(2)	98.66(8)
S(3)-Ni(2)-S(2)	169.16(7)	S(1)-Ni(2)-Ni(3)	132.99(6)
S(4)-Ni(2)-Ni(3)	48.58(5)	S(3)-Ni(2)-Ni(3)	48.81(7)

S(2)-Ni(2)-Ni(3)	123.84(8)	S(4)-Ni(3)-S(5)	179.01(7)
S(4)-Ni(3)-S(6)	97.80(8)	S(5)-Ni(3)-S(6)	83.19(8)
S(4)-Ni(3)-S(3)	81.29(8)	S(5)-Ni(3)-S(3)	97.76(8)
S(6)-Ni(3)-S(3)	169.67(7)	S(4)-Ni(3)-Ni(1)#1	130.99(6)
S(5)-Ni(3)-Ni(1)#1	49.84(6)	S(6)-Ni(3)-Ni(1)#1	49.90(6)
S(3)-Ni(3)-Ni(1)#1	123.63(7)	S(4)-Ni(3)-Ni(2)	48.38(7)
S(5)-Ni(3)-Ni(2)	131.11(7)	S(6)-Ni(3)-Ni(2)	123.54(6)
S(3)-Ni(3)-Ni(2)	48.82(5)	Ni(1)#1-Ni(3)-Ni(2)	113.68(6)

6. **Characterization Methods**

The powder X-ray diffraction was recorded on Bruker D8 Advance X-ray diffractometer in the 2θ range 5−50°. UV−vis absorption spectra were measured in the solid state using barium sulfate as the reference material on a SHIMADZU UV−vis/NIR (UV-2600) spectrophotometer. Ultraviolet photoelectron spectroscopy was performed in Omicron Nano tech. XPS. Thermogravimetric analysis (TGA) was performed using an SDT Q600 (Shimadzu) analyzer. The mass spectrum of the cluster samples were collected using Bruker microflex MALDI-TOF mass spectrometer. The matrix used was DCTB and a stock solution of DCTB was prepared with a concentration of 20 mg in 1 mL DCM. The sample was prepared as 1 mg in 10 μL DCM. From the stock solution, various 25 uL of matrix solution were taken and mixed with 1 μL of analyte solution with 0.1mg of silver triflouroacetate as ionizing source [reflective positive mode, 700 to 3500 m/z]. The molecules were ionized with the Nd: YAG laser (λ = 266 nm). The matrix concentration was varied for optimization to get a good resolved spectrum. Samples for C-AFM studies were prepared by dissolving compounds in Ethanol with a concentration of 2 mg/mL,

This solution was drop-casted on conducting FTO coated glass substrate (sheet resistance of 7 Ω/sq) to prepare thin films. AFM based studies were performed to observe film morphology in normal and conducting mode using pristine and annealed samples. Thin film sample was annealed at 130˚C for 15 minutes on hot plate under ambient environment. C-AFM also utilized to record current-voltage (*I-V*) characteristics for both the thin film samples to identify the difference in conductivity among them. These measurement were performed using a JPK Nanowizard Nanoscience AFM. Pt/Ir coated n-type doped silicon (Si) cantilever was used to record data in contact mode at a set point of 400mV. Obtained data were processed with JPK SPM Data processing software for further uses in this article. Topography and corresponding current mapping images were recorded simultaneously at the same area on the sample by applying a bias voltage of different values to the sample by keeping the tip grounded. A cleaned and bare FTO substrate also used to record topography and current mappng images as controlled experiment. Mostly, the RMS area roughness were calculated using the topographic images of scan area of (10 × 10 μm^2). Different locations on a particular sample were identified to record *I-V* characteristics by sweeping sample bias voltage starting from -2V to +2V (forward) and +2V to -2V (backward), successively. The same measurements were repeated for both pristine and annealed samples to identify their electrical property. The electrochemical impedance characterization was performed using PARSTAT 3000 A electrochemical workstation. It was done with three electrode system, where Ni-PET coated 0.075 cm dia glassy carbon and Ag/AgCl as working electrode and reference electrode respectively, graphite rod has served as a counter electrode. The Ni-PET cluster coating on electrode surface by drop caste method. For getting proper, impedance analysis, 1 mm in potassium ferricyanide 0.1 M sodium thio sulphate was used as redox mediator.

Mott-Schottky calculation of electron density

$$\frac{1}{C^2} = \frac{2}{\varepsilon_0 \varepsilon_r e_0 N_d}\left(V_{appl} - \frac{kT}{e_0}\right) \text{-----} (1)$$ [7]

$$Slope = \frac{2}{\varepsilon_0 \varepsilon_r e_0 N_d} \text{----} (2)$$

Where, C, ε_0, ε_r, e_0 and N_d are Capacitance (Farad), permittivity of free space (8.8541×10^{-12} $F.m^{-1}$), Relative permittivity (80.2), elementary charge unit ($1.602176634 \times 10^{-19}$ Coulomb) and charge carrier density on surface (m^{-3}).

Using dynamic impedance analysis, we have calculated the capacitance at various potential range from 0.6 V to 0.9 V in 0.1 M sodium sulphate solution, in this region, the compound is exhibiting only double layer capacitance (C_{dl}). Hence, we have fixed this region for this analysis. Utilizing the Mott Schottky equation 1, the plot $1/C^2$ *vs*. E(V) was done for the calculation of charge density on the surface and flat band potential. The negative slope of the graph conveyed that the compound is a p-type semiconductor. For understanding, all the important parameters tabulated shown in Table S3.

7. Computational Details

We performed the single-point calculation of the relevant dimer (extracted from the X-ray crystallographic data) using the DFT at the B3LYP level with the Gaussian 09 program package.[8] The Los Alamos effective core potential (ECP) $LanL_2$-DZ for the Ni atoms and split-valence 6-31G(d) basis set for the rest of the atoms were employed during optimization.[9,10] The non-covalent interaction was interpreted with the Bader's AIM approach and non-covalent interaction (NCI) method or reduced density gradient (RDG) method employing Multiwfn software package.[11] The electron density (ED) and bond critical point (BCP) provides the strength of the interaction between two atoms. For weak interaction, the electron density $\rho(rc)$ is quite small ($\sim 10^{-2}$ a.u. $\tau o \sim 10^{-2}$ a.u.) and the Laplacian of the electron density, $\nabla^2\rho$ (rc) is positive. Further reduced density gradient (RDG) or non-covalent interaction (NCI) index calculations were applied for the visualization of the attractive van der Waal's interaction. The color code denotes the attractive or repulsive interaction. Herein, the central green disk implied the weak S···S interaction, whereas blue and red regions indicated the strong covalent bonding (Metal-S bond) and strong electronic steric interaction in the cluster.

The projected density of states **(**PDOS**)** calculation for the compounds at the bulk level is carried out using Vienna Ab-Initio Simulation Package **(**VASP**)** by using Generalized gradient approximation of Perdew–Burke–Ernzerhof (PBE) functional.[12,13] Projector augmented wave (PAW) method is used for treating ion electron interactions.[14] The ionic relaxations have been carried out using a Conjugate gradient algorithm with convergence criteria of 10^{-4} eV for minimum energy and 0.05 eV $Å^{-1}$ for Hellmann-Feynman forces on atoms. Due to the large size of the unit cells of the compounds, the Brillouin zone was sampled at the Gamma point (1×1×1). For the PDOS calculation, a higher (2×2×2) K-point is used.

8. Characteristics figures

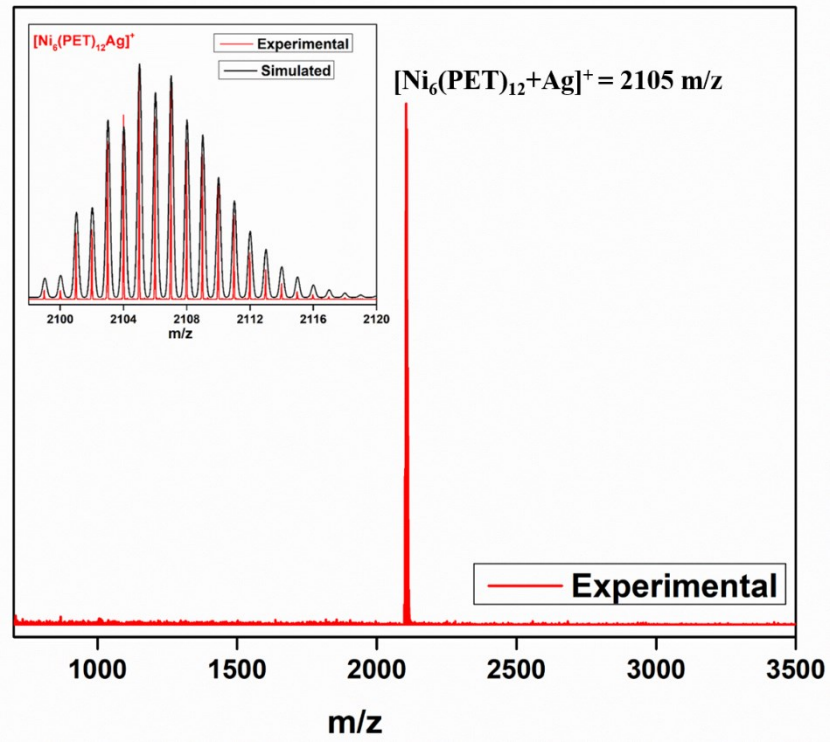

Figure S1: MALDI-MS showing the purity of the $Ni_6(PET)_{12}$ cluster. Inset: Isotopic pattern of simulated and experiment mass data of as-synthesized nickel cluster, respectively.
Note: silver triflouroactetate is used as cationizing source for obatining mass spectrum, where cluster is forming adduct with silver source.

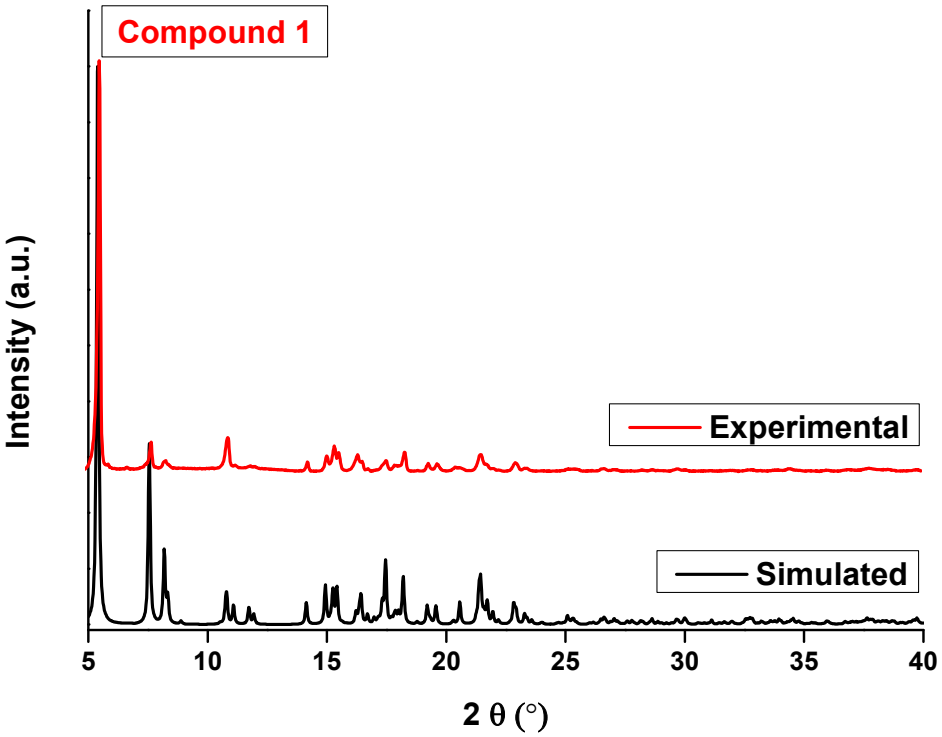

Figure S2: Experimental and simulated PXRD pattern of compound **1**.

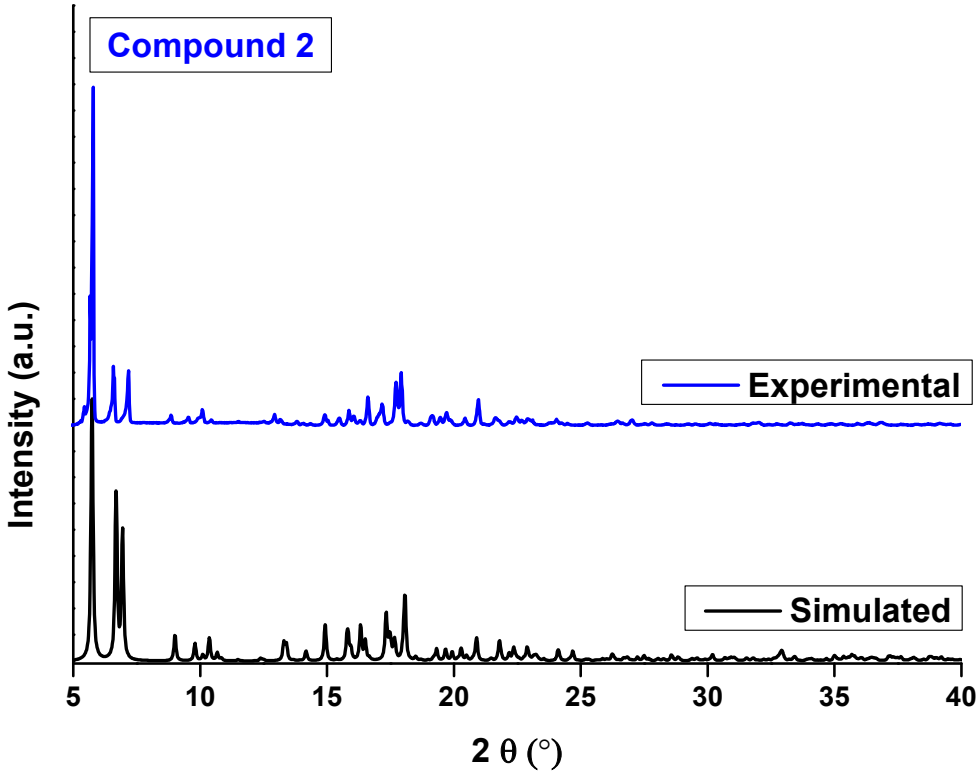

Figure S3: Experimental and simulated PXRD pattern of compound **2**.

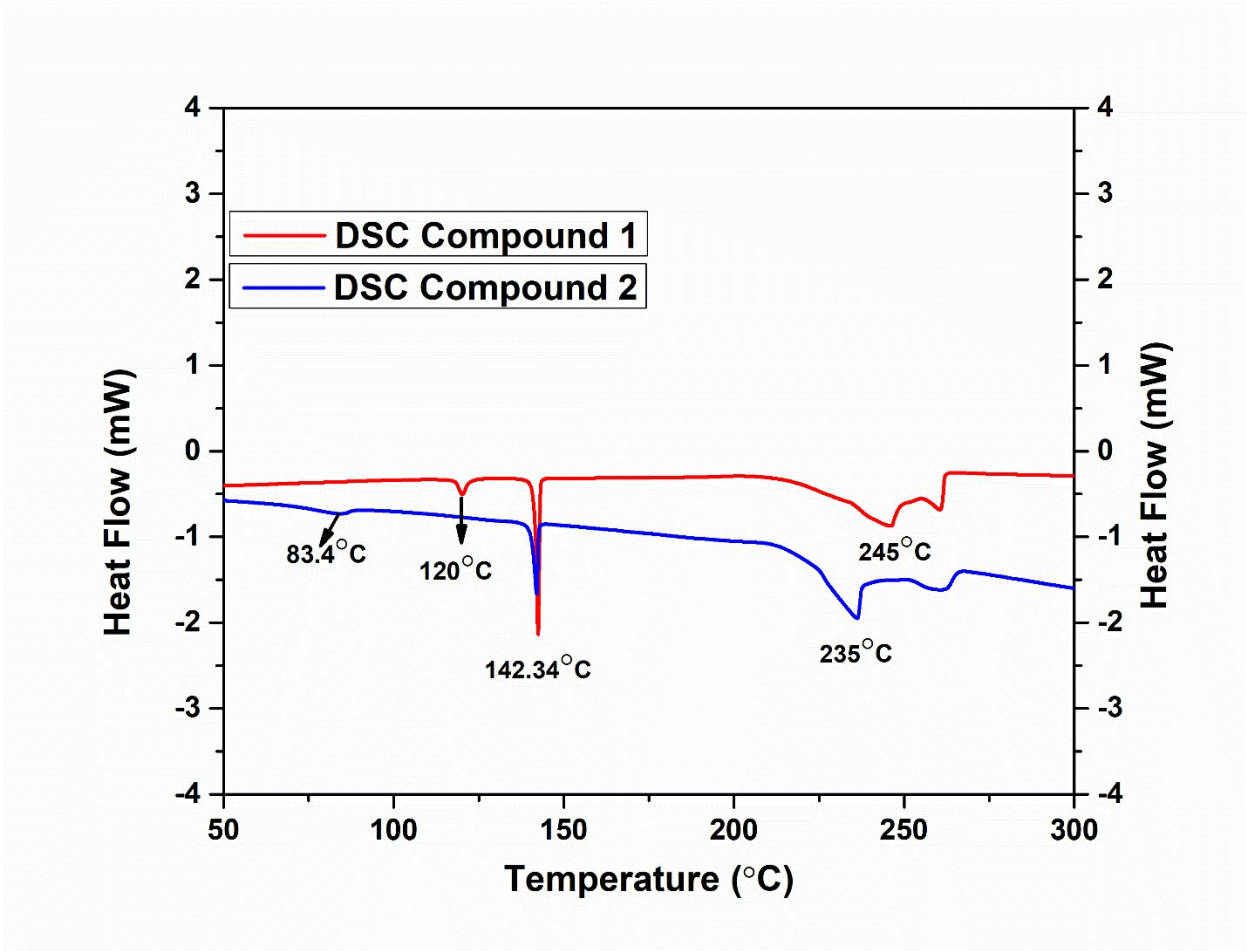

Figure S4. DSC plots of compound **1** and **2** respectively**.**

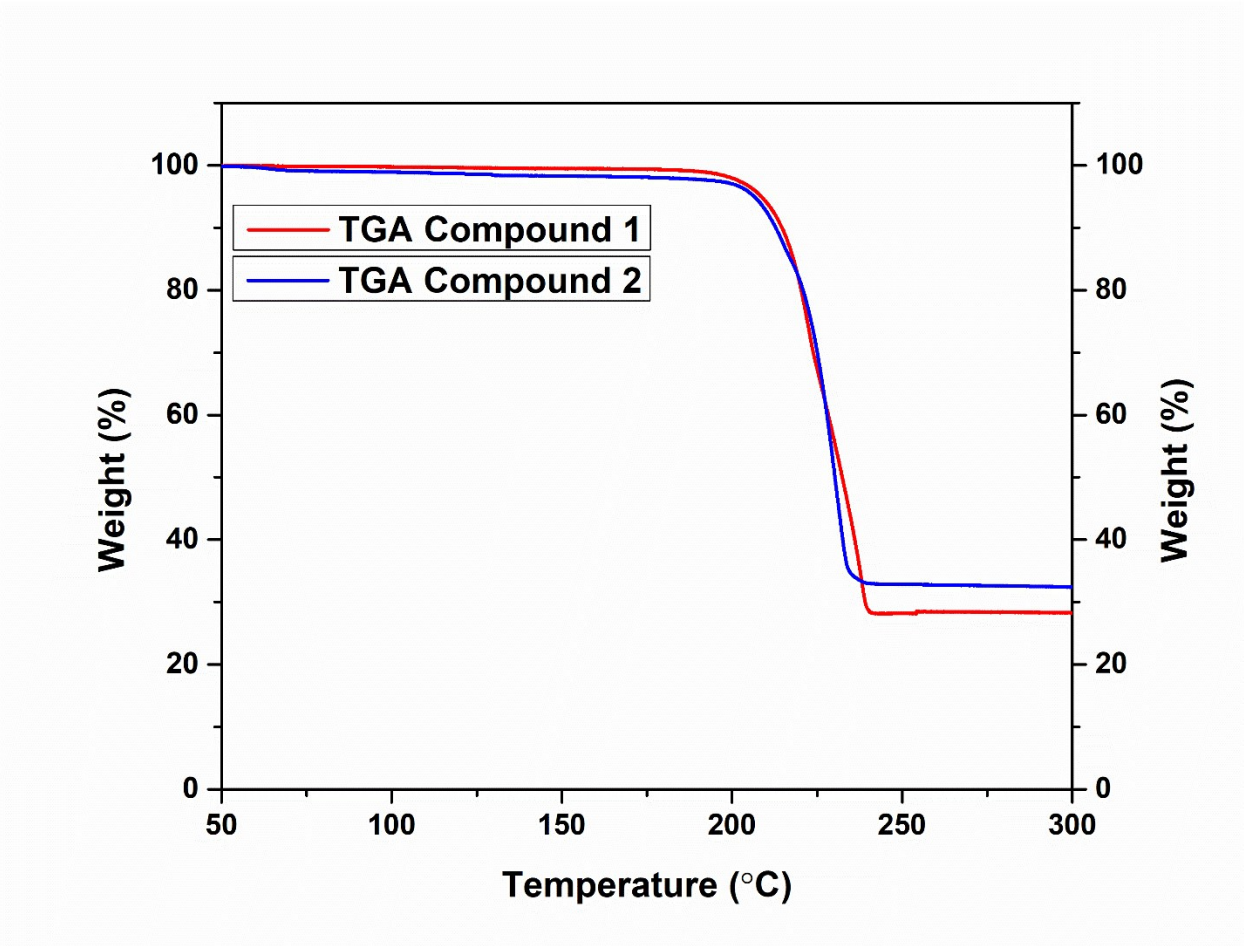

Figure S5. TGA plots of compound **1** and **2** respectively**.**

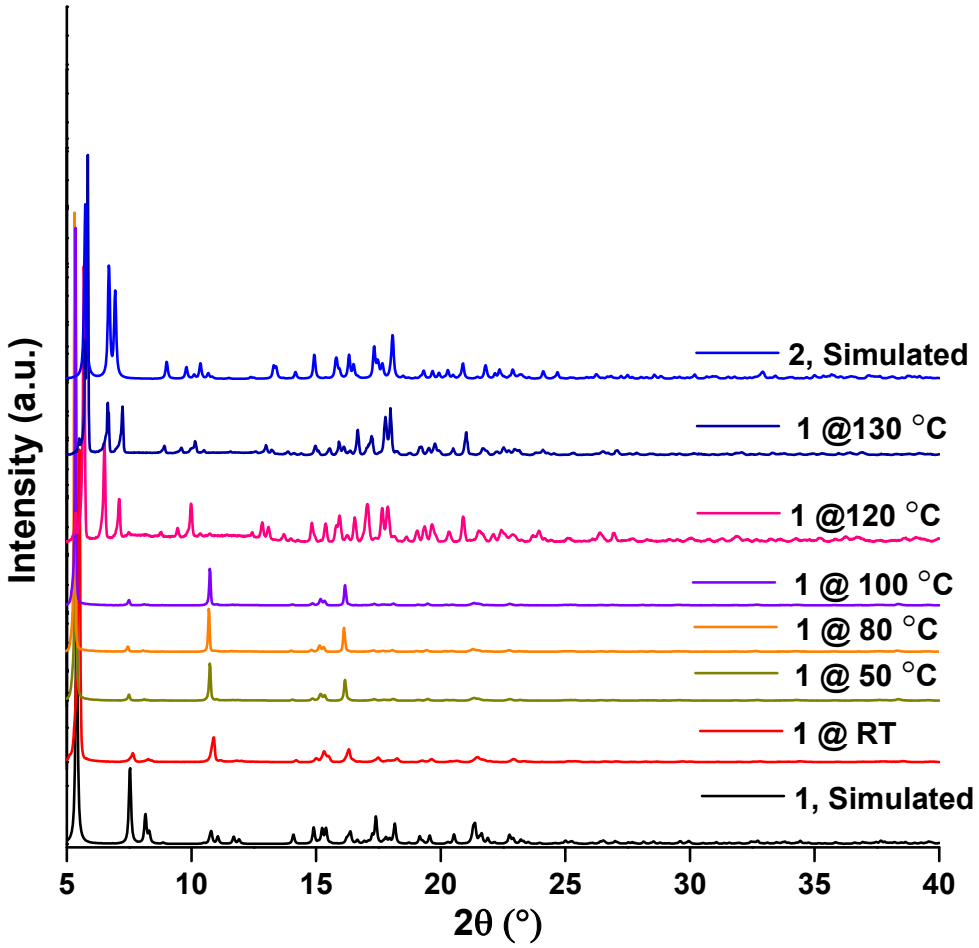

Figure S6: Temperature dependent PXRD pattern of compound **1**. Note that compound **1** converted to compound after heating at 130 °C.

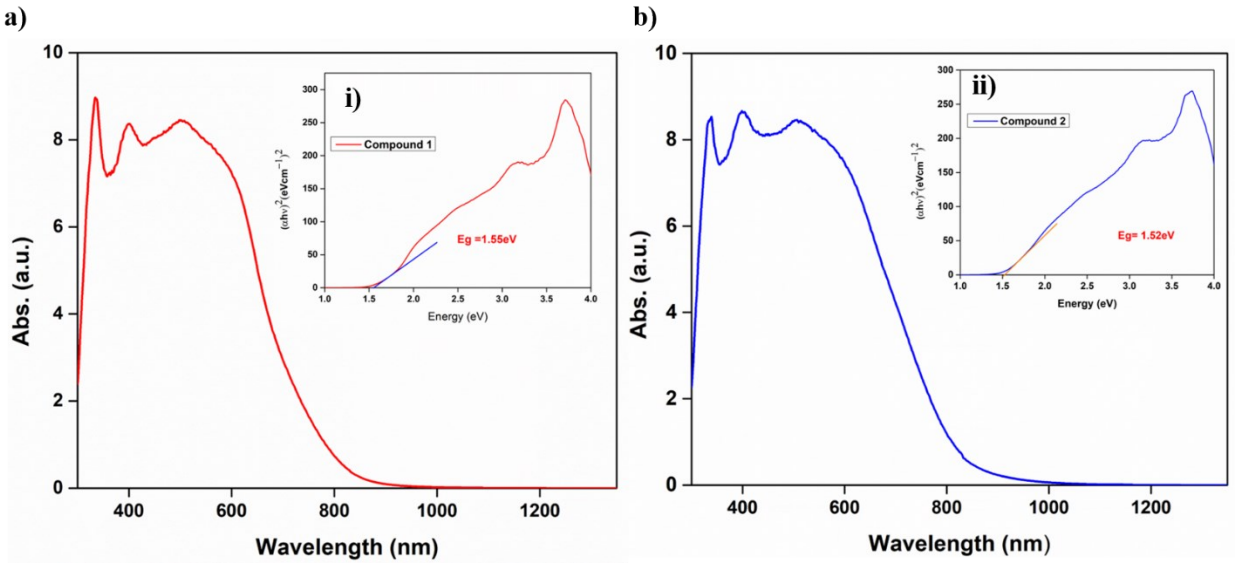

Figure S7: Solid state UV-Vis spectra of a) compound **1** and b) compound **2**, respectively. In set: Tauc plot of i) compound **1** and ii) compound **2**, respectively.

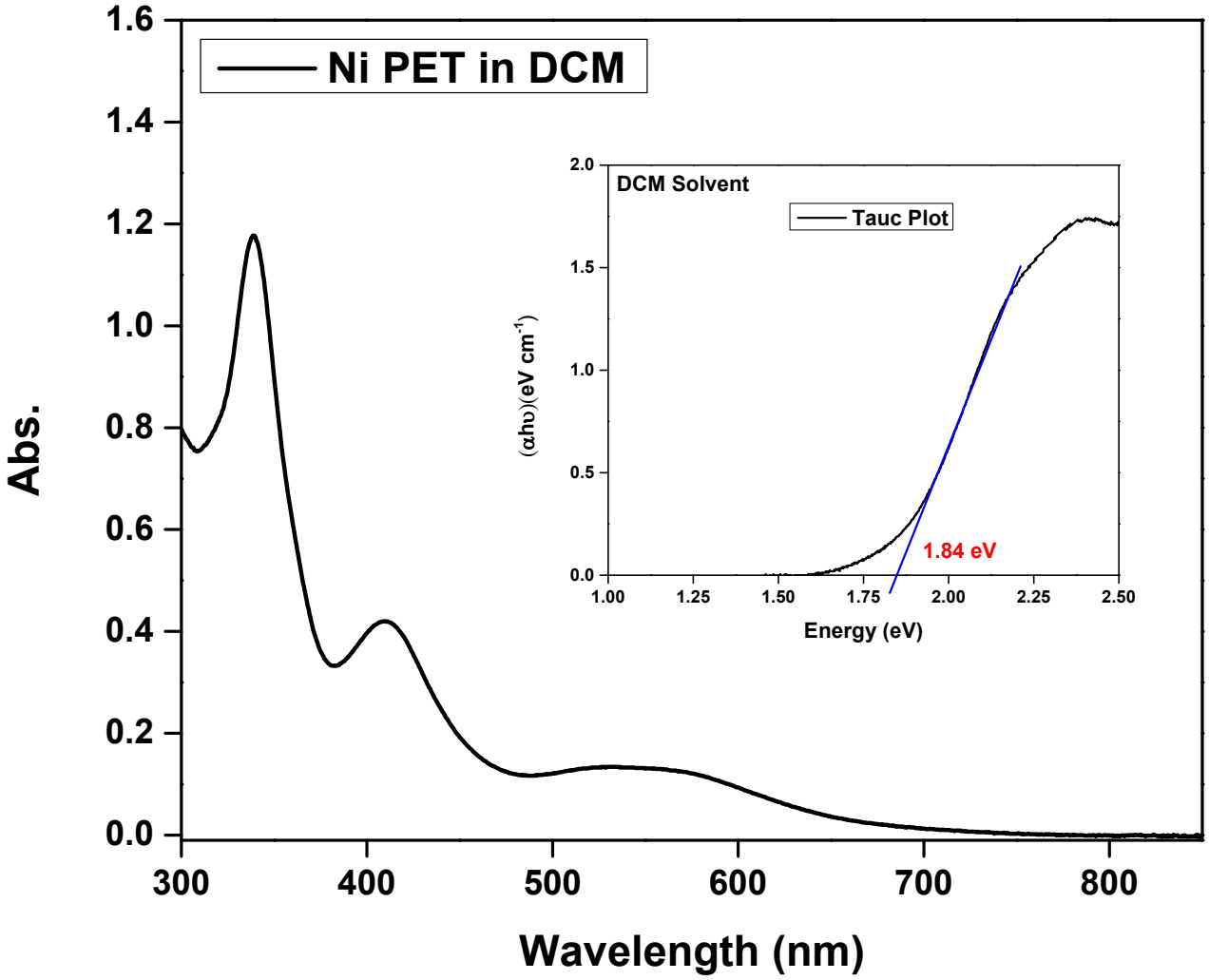

Figure S8: Absorption spectra of as-synthesized compound in DCM**.** Inset**:** Tauc plot of the same compound**.**

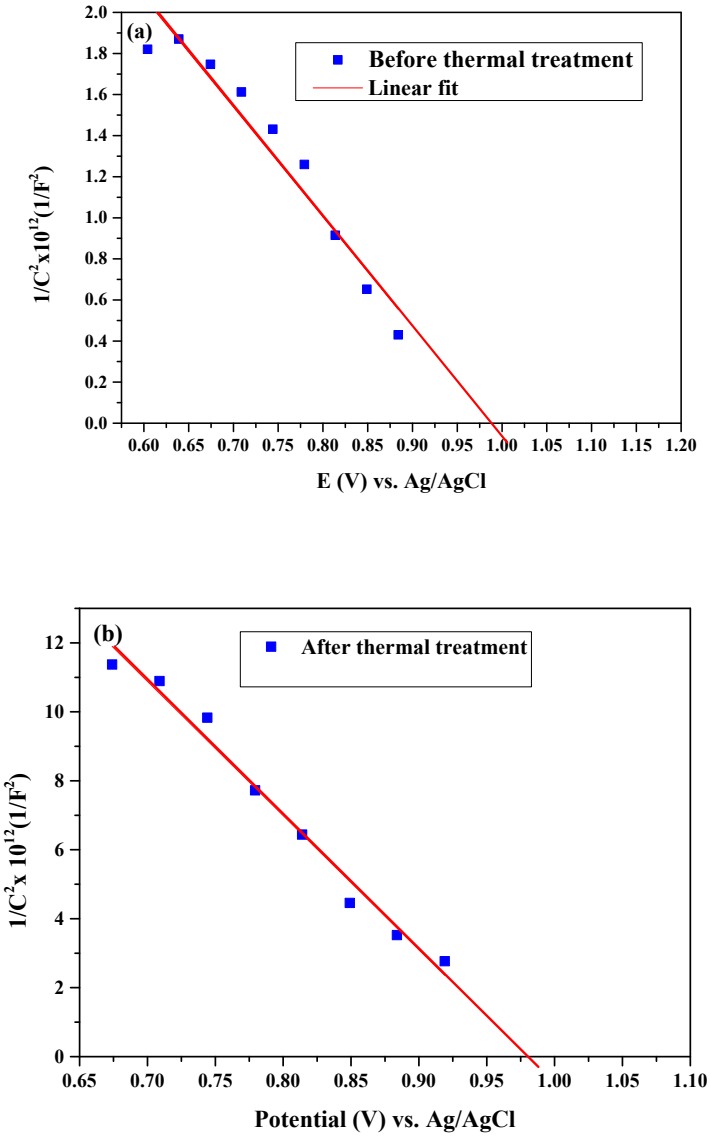

Figure S9. Mott-Schottky plot of $Ni_6[PET]_{12}$ (a) before heat treatment (compound **1**) (b) after heat treatment (compound **2**).

Table S3. Parameters obtained from the Mott-Schottky experiments.

S. No.	Compound	Slope (10^{12})	Flat band potential (V)	Hole density (m^{-3})
1.	Before heat treatment	5.35	0.989	6.8610×10^{25}
2.	After heat treatment	38.9	0.979	9.430×10^{24}

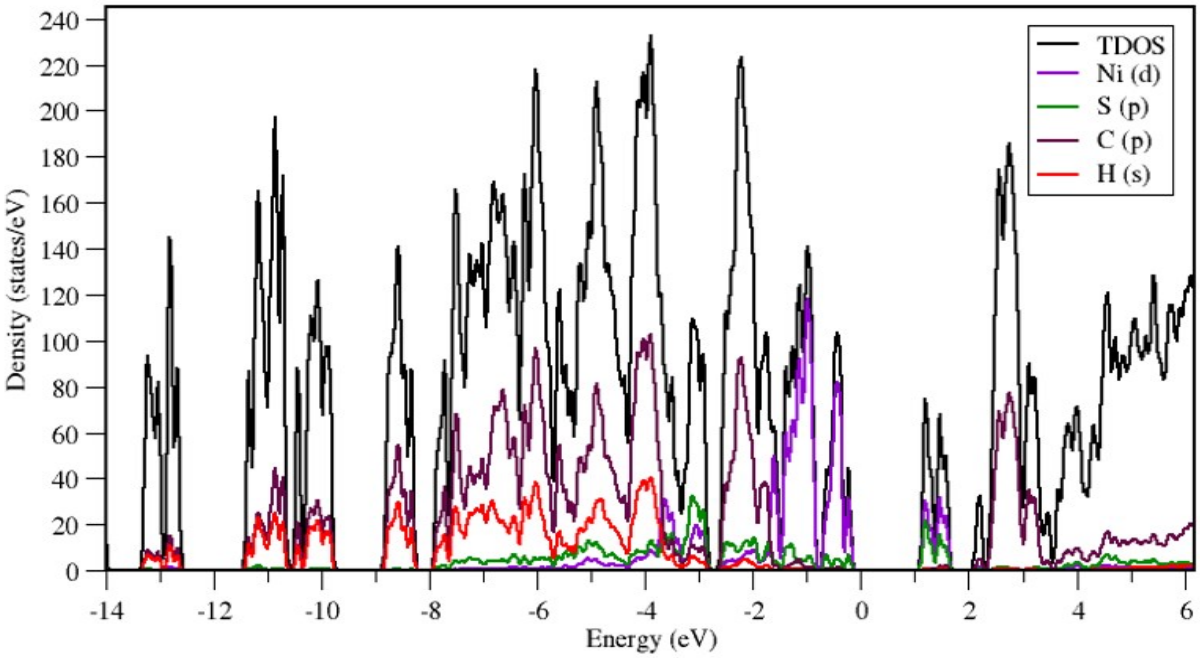

Figure S10. Projected Density of States of compound **1.**

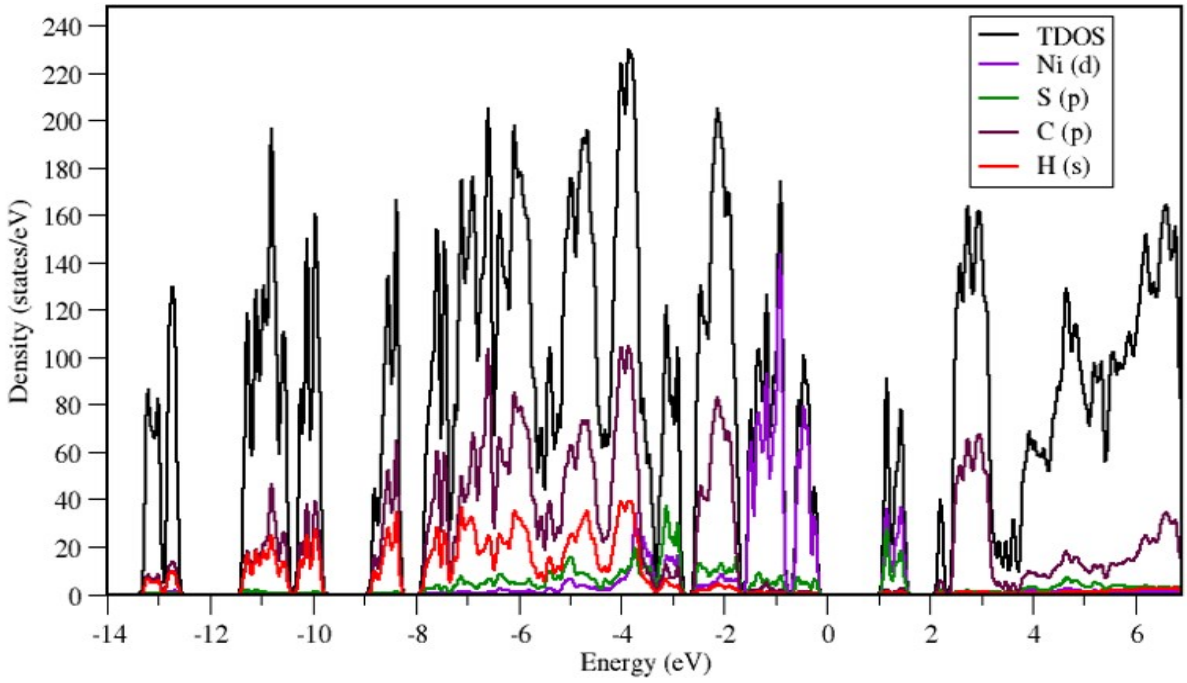

Figure S11. Projected Density of States of compound **2.**

(a) (b)

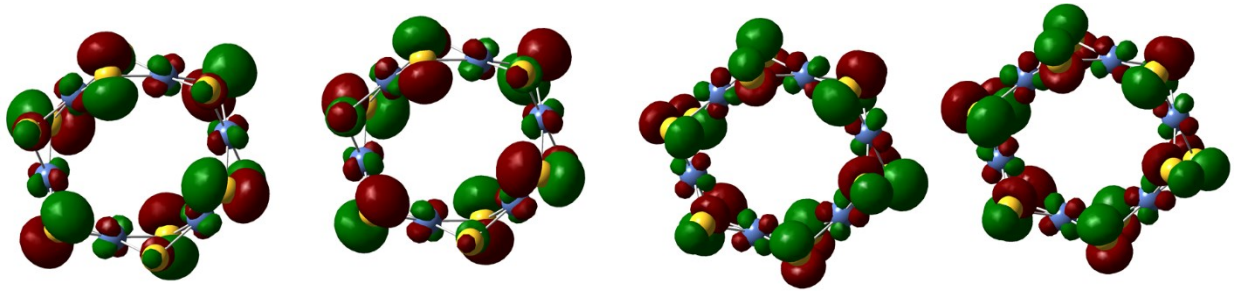

Figure S12. A pictorial representation of (a) HOMO and (b) LUMO of the activated dimer complex.

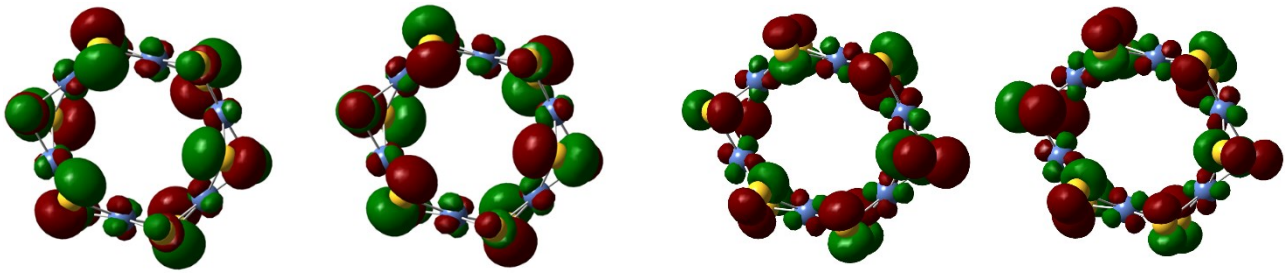

(a) (b)

Figure S13. A pictorial representation of (a) HOMO and (b) LUMO of the as-synthesized dimer complex.

Table S4. Band gap calculation from DFT study**.**

Structure	Band gap	HOMO position	LUMO position
Compound **1**	1.382 eV	0.7788 eV	2.1616 eV
Compound **2**	1.374 eV	0.7044 eV	2.0793 eV

(a) (b)

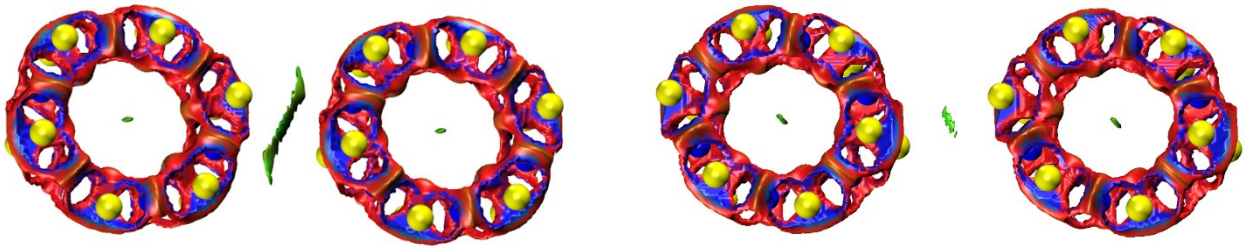

Figure S14. NCI iso-surface of **(**a**)** activated cluster and **(**b**)** pristine cluster**.**

The reduced density gradient **(**s**)** is a dimensionless quantity which is described as a deviation from homogeneous electron distribution, [15]

$$s = \frac{1}{2(3\pi^2)^{1/3}} \frac{|\nabla\rho|}{\rho^{4/3}}$$

The non-covalent interaction is denoted by the low electron density, ρ**(**r**)**, and low reduced density gradient, s**.** The color mapped iso-surface of RDG vs**.** sign **(**λ_2**)**ρ **[**λ_2 is the second Hessian eigenvalue**]** plot demonstrates the strong or weak as well as attractive or repulsive interaction**.** The negative value of sign **(**λ_2**)**ρ imply the attractive interaction and positive sign **(**λ_2**)**ρ denotes the repulsive interaction, such as steric interaction**.** The greater negative value of sign **(**λ_2**)**ρ indicates stronger bond strength as it contains more electron density **(**ρ**)** involved**.**

Table S5. The S····S distance, $\rho(r_c)$, $\nabla^2\rho$ (r_c), interaction energy (IE) of the pristine and activated dimer.

Cluster dimer	**S····S distance (Å)**	**$\rho(r_c)$ in a.u.**	**$\nabla^2\rho$ (r_c) in a.u.**	**IE (Kcal/mol)**
Pristine	4.070	0.002965	0.009035	– 0.69
Activated	3.795	0.004811	0.016139	– 0.87

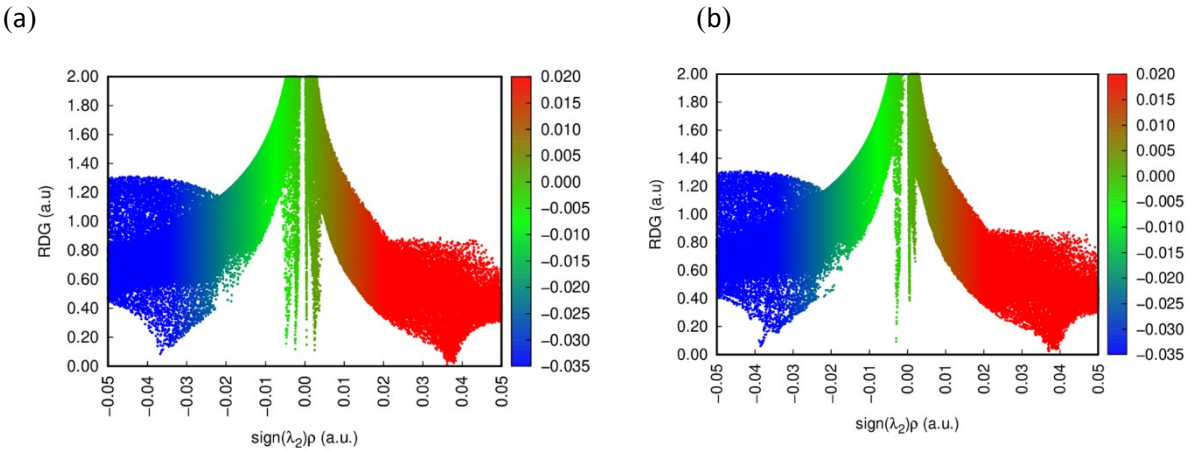

Figure S15. Reduced density gradient vs. sign $(\lambda_2)\rho$ plot of (a) activated (b) as-synthesized cluster.

In Figure S15, the green-colored spikes at negative sign $(\lambda_2)\rho$ indicate the weak attractive interaction involved between two clusters. The green spikes at more negative sign $(\lambda_2)\rho$ value in case of an activated compound than the as-synthesized one denotes stronger interaction of the former, as it has more electron density involved along the interaction path. Here, the blue and red regions indicate strong covalent bonding and steric interaction, respectively.

The interaction energy between the dimer was calculated using the equation,

$$\Delta E_{int}\,(AB) = E_{AB}\,(AB) - E_A\,(AB) - E_B\,(AB)$$

where, ΔE_{int} (AB) = interaction energy of the dimer, E_{AB} (AB) = total energy of the dimer, E_A (AB) = total energy of the monomer A calculated using dimer basis set, E_B (AB) = total energy of the monomer B calculated using dimer basis set.[16] This calculation was performed with B3LYP/LanL_2-DZ for the Ni atoms and split-valence B3LYP/6-31G(d) for other atoms in the Gaussian 09 program package.[7]

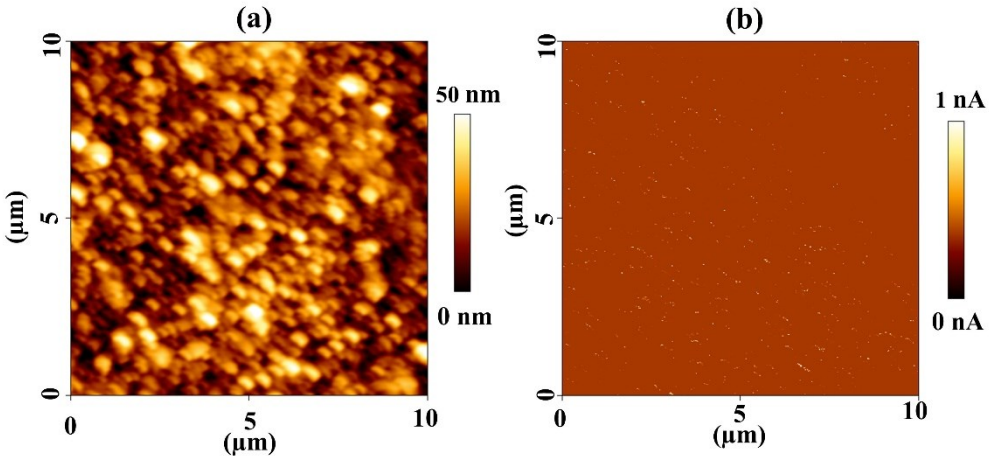

Figure S16. AFM topography (a) and current mapping (b) images of bare and cleaned FTO substrate recorded with a sample bias voltage +1.0V.

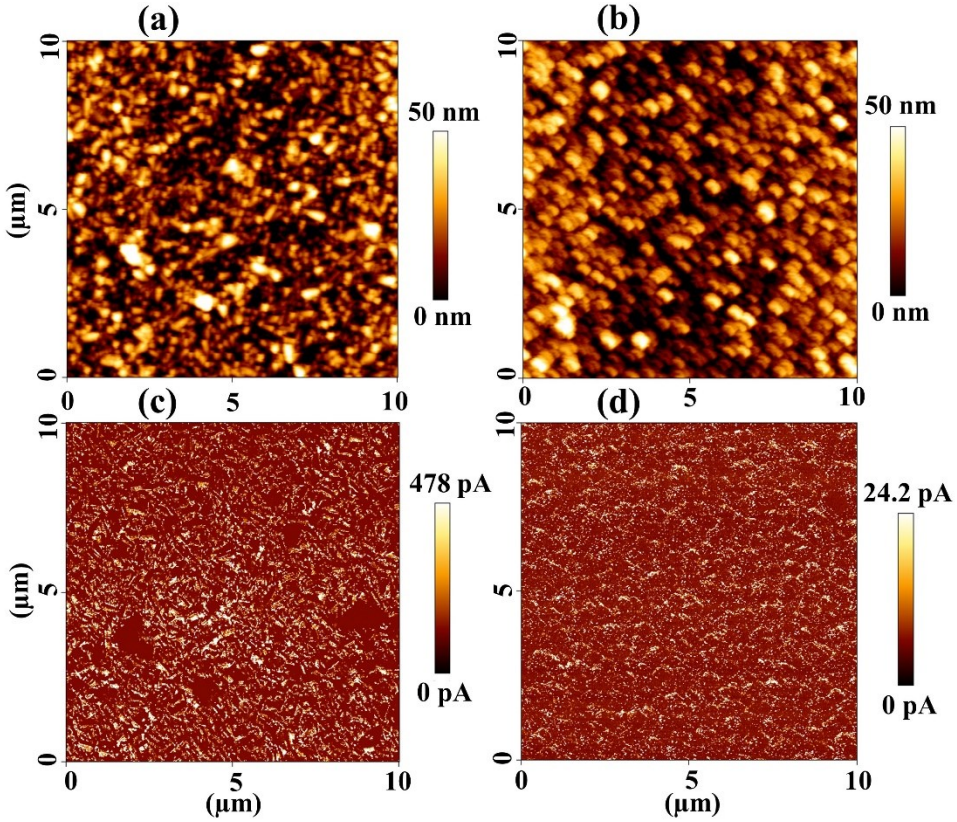

Figure S17. AFM topography images of pristine (a) and annealed (b) thin film of NiPET. (c & d) are their corresponding current mapping (C-AFM) images at a sample bias voltage +2V, respectively.

References

1. References

[1] Apex2, Version 2 User Manual, M86-E01078, Bruker Analytical X-ray Systems Madison, WI, 2006.

[2] G. M. Sheldrick, *SADABS 2016/2*; Bruker AXS, Inc.: Madison, WI, 2007.

[3] *Bruker SMART (5.059)* and *SAINT (6.01)*; Bruker AXS Inc.: Madison, Wisconsin, 1997.

[4] G. M. Sheldrick, SHELXT – Integrated Space-Group and Crystal-Structure Determination. *Acta Crystallogr*. 2015, **A71**, 3-8.

[5] G. M. Sheldrick, Crystal Structure Refinement with SHELXL. *Acta Crystallogr*. 2015, **C71**, 3-8.

[6] L. J. Farrugia, WinGX Suite for Small-Molecule Single-Crystal Crystallography. *J. Appl. Crystallogr*. 1999, **32**, 837-838.

[7] K. Gelderman, L. Lee, and S. W. Donne, *J. Chem. Educ*. 2007, **84**, 685.

[8] Frisch, M. J.; Trucks, G. W.; Schlegel, H. B.; Scuseria, G. E.; Robb, M. A.; Cheeseman, J. R.; Scalmani, G.; Barone, V.; Mennucci, B.; Petersson, G. A.; Nakatsuji, H.; Caricato, M.; Li, X.; Hratchian, H. P.; Izmaylov, A. F.; Bloino, J.; Zheng, G.; Sonnenberg, J. L.; Hada, M.; Ehara, M.; Toyota, K.; Fukuda, R.; Hasegawa, J.; Ishida, M.; Nakajima, T.; Honda, Y.; Kitao, O.; Nakai, H.; Vreven, T.; Montgomery, J. A., Jr.; Peralta, J. E.; Ogliaro, F.; Bearpark, M.; Heyd, J. J.; Brothers, E.; Kudin, K. N.; Staroverov, V. N.; Kobayashi, R.; Normand, J.; Raghavachari, K.; Rendell, A.; Burant, J. C.; Iyengar, S. S.; Tomasi, J.; Cossi, M.; Rega, N.; Millam, N. J.; Klene, M.; Knox, J. E.; Cross, J. B.; Bakken, V.; Adamo, C.; Jaramillo, J.; Gomperts, R.; Stratmann, R. E.; Yazyev, O.; Austin, A. J.; Cammi, R.; Pomelli, C.; Ochterski, J. W.; Martin, R. L.; Morokuma, K.; Zakrzewski, V. G.; Voth, G. A.; Salvador, P.; Dannenberg, J. J.; Dapprich, S.; Daniels, A. D.; Farkas, Ö.; Foresman, J. B.; Ortiz, J. V.; Cioslowski, J.; Fox, D. J.Gaussian 09 Revision C.01; Gaussian, Inc.: Wallingford, CT, 2010.

[9] Ab initio effective core potentials for molecular calculations. Potentials for the transition metal atoms Sc to Hg. *J. Chem. Phys.* **1985, 82**, 270.

[10] Ab initio effective core potentials for molecular calculations. Potentials for K to Au including the outermost core orbitals. *J. Chem. Phys.* **1985, 82**, 299.

[11] T. Lu, F. Chen, *J. Comput. Chem.,* 2012, **33**, 580.

[12] G. Kresse, J. Hafner, Ab initio molecular-dynamics simulation of the liquid metal−amorphous-semiconductor transition in germanium. *Phys*. *Rev*. *B*: *Condens*. *Matter Mater*. *Phys*. 1994, **49**, 14251

[13] J. P. Perdew, J. A. Chevary, S. H. Vosko, K. A. Jackson, M. R. Pederson, D. J. Singh, C. Fiolhais, Atoms, molecules, solids, and surfaces: Applications of the generalized gradient approximation for exchange and correlation. *Phys*. *Rev*. *B*: *Condens*. *Matter Mater*. *Phys*. 1992, **46**, 6671.

[14] G. Kresse, D. Joubert, From ultrasoft pseudopotentials to the projector augmented-wave method. *Phys*. *Rev*. *B*: *Condens*. *Matter Mater*. *Phys*. 1999, **59**, 1758.

[15] S. Mirdya, S. Banerjee, S. Chattopadhyay, An insight into the non-covalent Pb···S and S···S interactions in the solid-state structure of a hemidirected lead (II) complex. *CrystEngComm*, 2020, **22**, 237.

[16] Bader's Theory of Atoms in Molecules (AIM) and its Applications to Chemical Bonding. *J. Chem. Sci.*, 2016, **128**, 1527.